Environmental Science Advances

ROYAL SOCIETY OF CHEMISTRY

PAPER

View Article Online
View Journal | View Issue

Check for updates

Cite this: *Environ. Sci.: Adv.*, 2023, **2**, 652

Electrokinetic generation of iron-rich barriers in soils: realising the potential for nuclear site management and decommissioning†

Jamie M. Purkis,[a] Frances Burrell,[a] James R. Brydie,[b] James Graham,[c] Laurence Hopkinson[d] and Andrew B. Cundy *[a]

Following earlier field-scale pilot work on nuclear site materials in the late 2000s, there has recently been renewed research and industry interest in the application of electrokinetic technologies for nuclear site management and remediation in the UK. One relatively novel application of electrokinetics is the use of sacrificial steel electrodes (coupled with an *in situ* generated pH–Eh gradient in the treated material) to precipitate sub-surface iron-rich barriers for groundwater and/or leachate containment, which could be used to grout or contain contaminated fluids in the sub-surface on working nuclear sites or sites undergoing decommissioning. Here, we report previously unpublished data from two work programmes exploring the higher Technology Readiness Level (TRL) application of this electrokinetic iron-barrier approach to materials typical of those found in the subsurface of the Sellafield nuclear licensed site, UK. The first programme, funded by the UK National Nuclear Laboratory (NNL), assessed the electrokinetic generation of iron-rich barriers at metre + scale in simulated Sellafield materials, while the second programme, funded under the current UK TRANSCEND consortium project, examined electrokinetic iron-barrier formation at smaller (<1 m) scale, but in real site materials. Both programmes indicate that iron-rich barriers can be conveniently and electrokinetically grown in different geometries over reasonable timescales (months) in realistic site subsurface materials (sands), in electrolytes similar to natural waters found in the environment. Voltage requirements are low (<1 V cm^{-1}) with energy and consumables costs of no more than single-digit or tens of US dollars at the metre-plus scale. Further work is needed however to assess the longevity of the iron precipitates forming the subsurface barrier, and to explore barrier generation at the geometries and scales required for (site specific) field application.

Received 6th December 2022
Accepted 28th February 2023

DOI: 10.1039/d2va00308b

rsc.li/esadvances

Open Access Article. Published on 06 marzu 2023. Downloaded on 17/10/2025 12:44:53.
This article is licensed under a Creative Commons Attribution 3.0 Unported Licence.

Environmental significance

Working nuclear sites (and those undergoing decommissioning) provide a range of serious environmental challenges, including management of contaminated groundwaters and liquid waste spillages. Following earlier work on nuclear site materials in the 2000s, there has recently been renewed research and industry interest in the application of electrokinetic technologies for nuclear site management and decommissioning, particularly for wastes and groundwater management *via* stabilization and grouting, or subsurface barrier generation. Here, we assess and generate *in situ* electrokinetically-grown iron barriers at scale, using simulated and real material from an internationally-important nuclear site, for the first time. By providing new insights into scalability we make these *in situ* barrier technologies, which mimic natural iron mineralization processes, potentially attractive options for risk mitigation at nuclear sites.

1. Introduction

Electrokinetic remediation (EKR) is a potentially valuable addition to the engineer's toolbox of technologies for the treatment of contaminated soils and wastes, where organic and/or inorganic contaminant species are force-migrated through a natural or anthropogenically-modified material using an applied electric field. The technique works in a variety of low-permeability substrates including inhomogeneous, low-permeability (*e.g.* clayey) soils, can be applied *ex* or *in situ*,[1] and has been used by a range of groups for the treatment of metal,[2] organic[3] and radioactively[4] contaminated materials. Alongside other *in situ* technologies (*e.g.* phyto- and bio-remediation, permeable reactive barriers, *etc.*), EKR offers significant advantages over *ex situ* technologies (*e.g.* excavation, pump-and-treat), as (for *in situ* technologies) the need to physically handle and transport materials is minimized. At sites with radioactive contamination, for

[a]GAU-Radioanalytical, School of Ocean and Earth Science, University of Southampton, National Oceanography Centre (Southampton), European Way, Southampton, SO14 3ZH, UK. E-mail: A.Cundy@soton.ac.uk

[b]CanmetENERGY, Natural Resources Canada, Devon, Alberta, T9G 1A8, Canada

[c]National Nuclear Laboratory, Central Laboratory, Sellafield, Seascale, Cumbria, CA20 1PG, UK

[d]School of Applied Sciences, University of Brighton, Lewes Road, Brighton, BN2 4GJ, UK

† Electronic supplementary information (ESI) available. See DOI: https://doi.org/10.1039/d2va00308b

© 2023 The Author(s). Published by the Royal Society of Chemistry

Open Access Article. Published on 06 marzu 2023. Downloaded on 17/10/2025 12:44:53.
This article is licensed under a Creative Commons Attribution 3.0 Unported Licence.

example, this is vital where worker safety is a top priority.[4] Further, where the physical removal of contaminated material is not possible (*e.g.* for contaminated buried (geological) materials or soil under a structure), EKR may still be applied. Although the remediation timeframe may be longer than for *ex situ* methods, the cost is anticipated to be lower, which is important for large, site-scale, treatment.

In addition to conventional EKR, one promising avenue for EKR technology is the combined forced migration of contaminants plus *in situ* precipitation of mineral barriers. With increasing barrier precipitation, permeability decreases, which allows for manipulation of local-scale hydraulic conditions, and possible containment of contaminated groundwater or leachates. Ferric iron remediation and stabilisation (FIRS) is a technology developed and patented[5] in 2007 that deliberately corrodes stainless or mild steel electrodes (using direct current) to do this. Iron (as Fe^{2+}) leached from a sacrificial anode(s) migrates between electrodes in the pore space of contaminated substrates and is oxidized and precipitates as it encounters the pH gradient developed during the EKR process (Fig. 1). The soil mineralogy, grain size boundaries and fluid flow all influence the growth of these mineral phases, whereby clay promotes amorphous iron-rich 'pans',[6] and sands and silts encourage the coating of soil particles with sorptive,[7] iron-rich coatings.[8] These iron phases may be generated remotely in the subsurface in a number of configurations or geometries, depending on electrode design and placement, forming a physical barrier to groundwater flow or stabilizing and strengthening soils.[9] Authigenic iron-rich phases are common in surface and subsurface materials, for example, forming Fe-rich "pans" in soils, or Liesegang-like bands, which are alternating iron-rich, iron-poor rings extending radially and concentrically from a central core; these are important as they can influence hydro(geo)logy at or around a given site.[10] Iron bands or barriers in soils, particularly when grown deliberately, are therefore important as they influence flow paths and therefore contaminant transport.

A schematic for the growth of electrokinetically generated iron-rich phases in soils is given in Fig. 1. Iron, from anode corrosion, migrates towards the cathode before precipitating at the pH–Eh "front" generated by the electric potential (which can range from *ca.* pH 2 in the acidic zone to >pH 10 in the alkaline zone) in the treated soil, sediment or waste material. The form of iron precipitated depends on the solution pH, soil type, dissolved oxygen, *etc.*, and the precipitated species/minerals can include goethite (α-FeO(OH)), lepidocrocite (γ-FeO(OH)), elemental iron (Fe^0), maghemite (γ-Fe_2O_3), magnetite (Fe_3O_4, $(Fe^{2+}Fe^{3+}{}_2)O_4$), and limonite ($FeO(OH)\cdot nH_2O$; n is an integer). Other crystalline and amorphous iron oxyhydroxides (rusts, green rusts,[11] *etc.*) are also possible.[6,9] These phases are effective adsorbents of a range of contaminants and their surfaces are redox active[12] (potentials ranging from −0.5 to +1.1 V *vs.* the standard hydrogen electrode, SHE),[13] making iron-rich barriers grown *in situ* a potentially attractive technology for (a), containment and management of contaminated groundwater or leachates, and (b), *in situ* sorption or reductive precipitation of contaminants onto these iron-rich phases.[14–23] Following cessation of applied current the pH gradient dissipates, leaving a solid Fe-rich barrier that can be extracted, or left in place in the subsurface.

In 2005 Faulkner *et al.* demonstrated that impermeable ($<10^{-9}$ m s^{-1}) iron-rich barriers could be grown at laboratory scale in both vertical and horizontal arrangements.[9] Additional work by Cundy and Hopkinson (2005)[6] expanded this to the treatment of ^{60}Co-contaminated estuarine deposits near the Sellafield facility, Cumbria, UK. Low voltage (<0.2 V cm^{-1}) iron-barrier growth (over 17 days) offered significant enhancements in sediment shear strength (which increased from <0.5 to 20 kN m^{-2}) and mechanical strength (final unconfined compressive strength of 10.8 N mm^{-2}, equivalent to sandstone), with the removal of up to 50% of ^{60}Co in contaminated sediments. EKR and FIRS have also been demonstrated to be effective in the treatment of Cr^{6+} contaminated wastes, *via* electrokinetic iron injection.[12]

Moving from the laboratory to the field and (finally) routine site scale application however remains a key limitation to EKR techniques, with more studies required at larger scale, to determine the scalability, applicability, reliability and cost-effectiveness of EKR for site remediation.[25,26] Here, we report the remote precipitation of iron-rich barriers, in (i) controlled

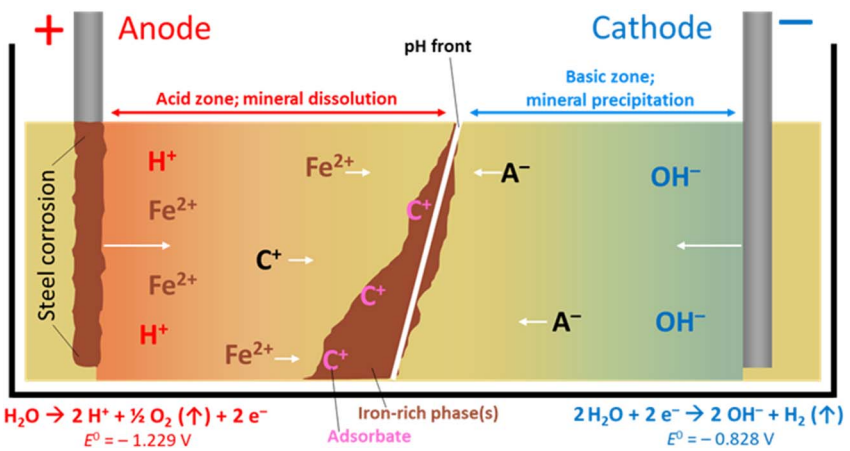

Fig. 1 The FIRS process, with precipitation of iron-rich phases. Cation (C^+) and anion (A^-) movement with pH gradient, towards electrodes of opposing charge, is shown. Water electrolysis half-cell values are *vs.* SHE. The oxidation of ferrous to ferric iron (Fe^{2+} to Fe^{3+} $E^o = -0.771$ V *vs.* SHE)[24] typically occurs by diffusion of dioxygen through interstitial pore waters. System uses direct current application.

Open Access Article. Published on 06 marzu 2023. Downloaded on 17/10/2025 12:44:53.
This article is licensed under a Creative Commons Attribution 3.0 Unported Licence.

geometries in metre-plus cells, and (ii) silica-rich subsurface materials from the UK's Sellafield nuclear facility, Cumbria. We incorporate the results of previously unpublished industrial research, conducted between 2003–2007, which have been released for this paper, and supplement this with recent work (2020–2022) carried out in the ongoing UK TRANSCEND (TRANsformative SCience and Engineering and Nuclear Decommissioning) project, which brings together 11 UK Universities and 8 industry partners to carry out fundamental and applied research to support innovative technology developments in nuclear decommissioning and waste management. We conclude by assessing the potential wider application of EKR barrier technologies in nuclear site management and decommissioning, for example, in the immobilization of site contaminants in the subsurface and/or used as hydraulic containment techniques, at field scale.

2. Materials and methods

2.1 Overview

The work described here was undertaken by a number of organizations, including the predecessor organizations of the National Nuclear Laboratory (NNL), Nexia Solutions, British Nuclear Fuels Ltd (BNFL), C-Tech Innovation Ltd (under contract to Nexia Solutions) between 2003 and 2007 and, separately, the University of Southampton (2020–2022), in two programmes of research assessing the potential for combining EKR with *in situ* barrier precipitation for nuclear site application, using simulated and real subsurface materials from the UK's Sellafield nuclear site as a case study. We summarize this work below, dividing it into two sections: bench-top (<0.5 m dimension) on real site materials, and large-scale (>1 m dimension) experiments on simulated site materials. Unless specified all materials were from commercial suppliers and used without treatment.

2.2 Bench-scale experiments using real site materials

To assess the *in situ* growth of iron barriers in real site materials, and the role of electrolyte composition and ionic strength on barrier precipitation and growth rate, 1.25 kg of site sands were added to separate clear polypropylene plastic cells (LWH = 19 × 13 × 9 cm). This material was collected from the Peel Place quarry (Holmrook, Cumbria, UK, CA19 1YD) – located close to (and in hydraulic and geological continuity with) the Sellafield site, within similar Quaternary superficial deposits to those found underlying the Sellafield site. The sands were dominantly quartz in composition, with orthoclase and plagioclase feldspar – Fe concentrations were *ca.* 0.9%, dominantly in oxide phases (Fe data provided by the University of Manchester, unpublished data).

Two steel electrodes (Meehanite type SF 60 ferritic steel; length 229 mm, diameter 15 mm) were added at either end of the cells (separation = 17 cm), and voltage applied over time *via* crocodile clips connected to the electrodes and a Farnell dual power supply set to 10 V DC (0.53 V cm^{-1}). Several experiments were carried out using electrolytes of different composition and ionic strength, either tap water (from the mains water supply at the University of Southampton; 'hard' water, *ca.* 115 mg $CaCO_3$ per L), or 20, 100 or 500 parts per million (ppm) potassium chloride (reagent grade, Sigma-Aldrich) solutions in MilliQ grade deionized water. Control cells containing only the electrodes with deionized water, tap water or 500 ppm KCl and no voltage were also used.

We selected these concentrations to provide a range of environmentally-relevant groundwater conditions,[27] as well as tap water, which is readily available with a specific conductivity (405 μS cm^{-1}) similar to groundwater at the Sellafield site (350–400 μS cm^{-1}).[28] Variable amounts of electrolyte (typically 50–150 mL) were added as needed to maintain saturation in all cells. Temperature-corrected conductometry was performed using a WTW 340i multimeter and A325 conductometry probe. Current (amperometer) was measured from the digital display on the power supply at 1 mA resolution. The typical set-up for these experiments is shown below in Fig. 2.

2.3 Large-scale experiments, using simulated site materials

To study the growth of electrokinetically-generated iron-rich barriers at larger scale (*e.g.* metre-plus), a 2 × 1 × 1 m (LWH; 2 m^3) tank was filled with 3050 kg of silica sand. The cell was saturated with 700 L of 1 mM $NaNO_3$ electrolyte and left to stand for 5 days to ensure complete settling. The sides of the container were transparent Perspex®, to allow the water level and iron barrier growth to be observed. Silica sand was selected as the

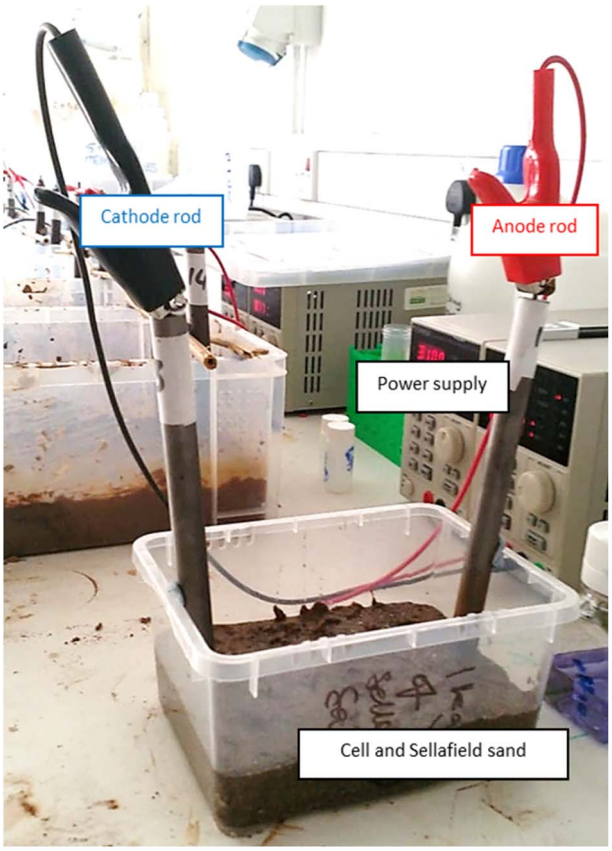

Fig. 2 Bench-scale apparatus used for electrolyte conductivity and iron barrier growth experiments, exemplified here with the cell containing 500 ppm KCl.

© 2023 The Author(s). Published by the Royal Society of Chemistry

Open Access Article. Published on 06 marzu 2023. Downloaded on 17/10/2025 12:44:53.
This article is licensed under a Creative Commons Attribution 3.0 Unported Licence.

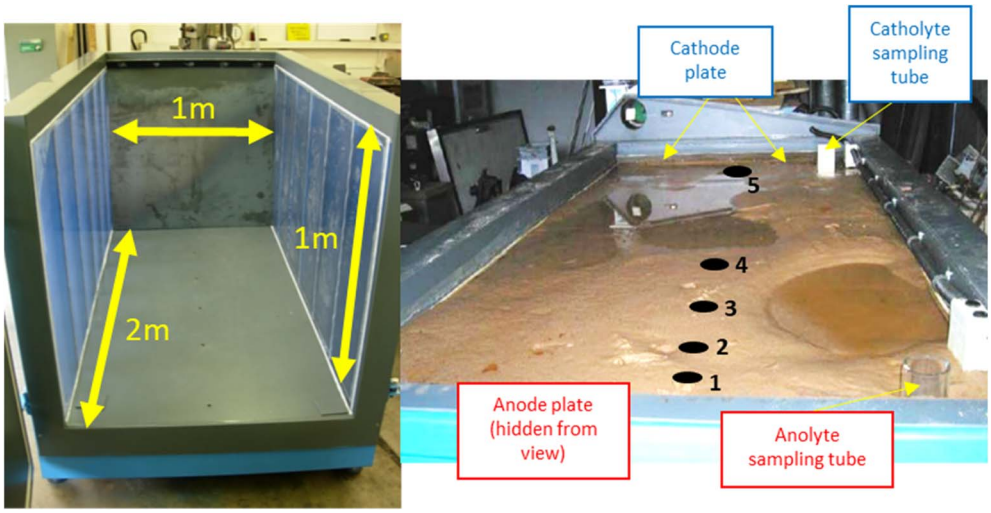

Fig. 3 Left, dimensions of the empty cell with blue-tinted translucent Perspex® windows visible on either side of the cell; right, cell in operation with saturated sand. Cathode and anode electrode plates are highlighted, as are electrolyte sampling tubes. Electrolyte solution (1 Mm $NaNO_3$) was added as necessary to anolyte or catholyte sampling tube to counter evaporation during the experiment. Numbers 1–5 indicate pH sampling sites at selected distances from the anode including, 10 cm, 30 cm, 45 cm, 80 cm, and 182 cm, respectively. A schematic complete with pH measurements is given in Fig. 5.

substrate to ensure adequate and homogenous porosity and permeability throughout the cell. Electrolyte sampling tubes (high-density polyethylene, HDPE, plastic perforated along tube) were added to enable pore solution aliquots to be taken for pH measurement. 1 mM $NaNO_3$ electrolyte was added as required, to ensure constant saturation was maintained. Fig. 3 shows the cell both empty and in operation. The experiment ran for a total of 160 days.

Mild steel anodes and stainless steel cathodes were arranged as parallel plates, using a 50 V potential difference (0.25 V cm^{-1}). Aliquots of electrolyte (1 L) were also taken from sampling tubes and the cell after the experiment concluded, to determine the pH of the electrolyte solution from selected points.

3. Results and discussion

3.1 Iron barrier growth

Iron barrier formation was observed in both real and simulated site materials, at both experimental scales (Sections 2.2–2.3). The time required to visually observe the first appearance of the iron barrier material reflected both the experimental scale and voltage applied, but also electrolyte strength: in the larger-scale experiment (2 m long, 50 V) iron barrier precipitation was observed after 6 weeks (42 days), while the bench-scale experiments showed iron barrier precipitation within 30 days (for higher ionic strength electrolytes – N. B. the effect of electrolyte strength on barrier growth rate and position is discussed further in Section 3.2).

In the bench-scale cells, a sub-vertical iron-rich barrier was generated in all experiments, towards the anode side of the cell (3–30 mm from the anode – see Section 3.2). The iron barrier grown in the large cell was *ca.* 160 cm across, extending horizontally across four-fifths of the cell from the anode (Fig. 4 and 5). Significant amounts of material also formed at the bottom of the cell. In such a well-mixed, homogeneous and porous system this is probably the result of gravitational settling of iron precipitates, which in more heterogeneous systems would tend to accumulate at permeability/grain size boundaries, and/or

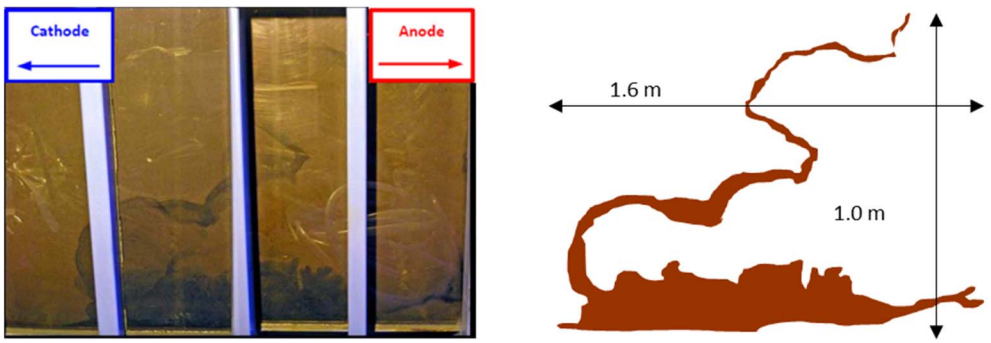

Fig. 4 Left, view of the precipitated iron barrier through the Perspex® plastic sides of the large scale experiment; right, superimposable schematic of the iron barrier with approximate dimensions.

Open Access Article. Published on 06 marzu 2023. Downloaded on 17/10/2025 12:44:53.
This article is licensed under a Creative Commons Attribution 3.0 Unported Licence.

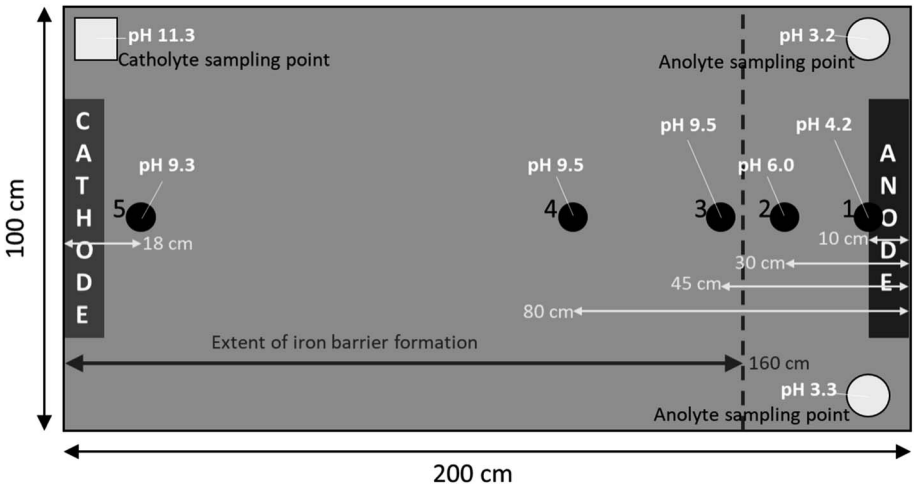

Fig. 5 Extent of iron barrier formation across cell and pH measurements in the large-scale cell on day 160, the end of the experiment. See Fig. 3 for the cell in operation.

enhanced electrode corrosion at depth (ref. Fig. 6). Data for pH, collected between sampling points 2 and 3 at the end of the experiment, confirm conditions are sufficiently alkaline (*e.g.* ≥pH *ca.* 6) to precipitate dissolved iron (Fig. 5). This follows the known redox chemistry of Fe^{2+}, where, depending on the redox potential, a pH of between 5 and 7 is normally sufficient to cause precipitation.[29] Galvanic corrosion of the plate electrodes from a pilot smaller-scale experiment (described in ESI†), shown in Fig. 6, provides additional insights into the mechanism of iron barrier growth.

The extent of corrosion is clearly visible, with two distinct bands formed below the level of electrolyte saturation. Iron (electro)chemistry in oxic, anoxic and hypoxic environments is complex. Possible reactions for the initial electro-corrosion of

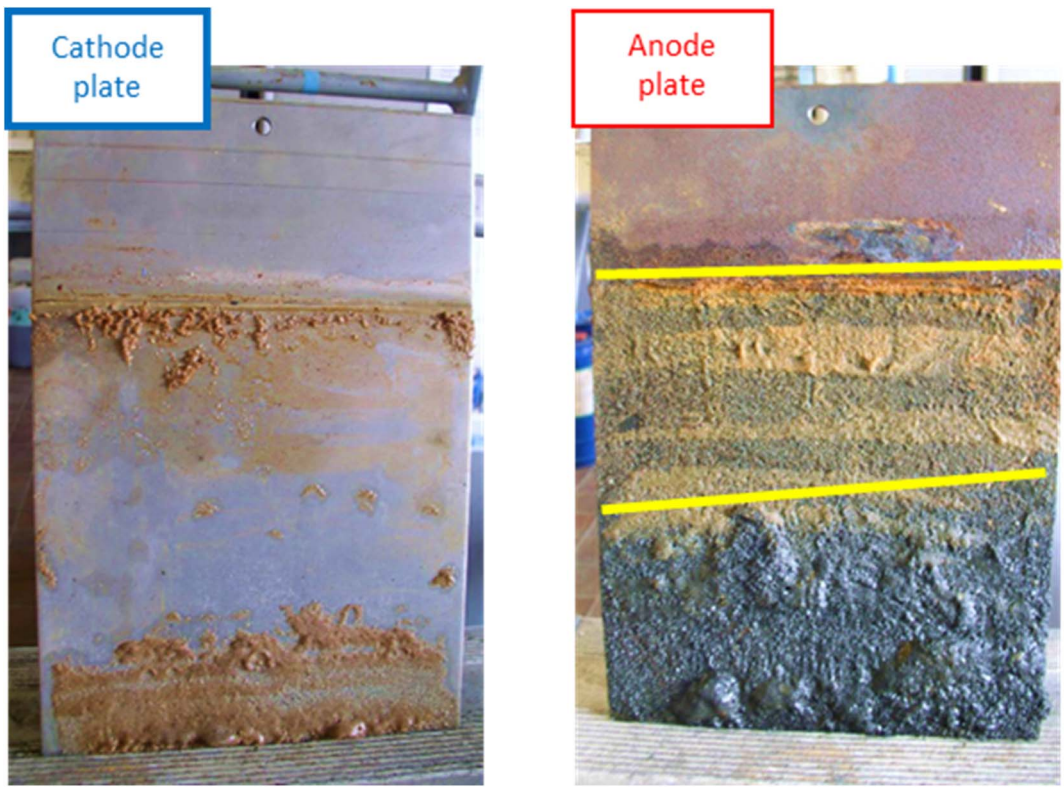

Fig. 6 Cathode (left) and anode (right) plates from a pilot scale experiment (described in ESI†), conducted to inform set-up of the large-scale experiment, showing the difference in galvanic corrosion. The distinct bands of material are highlighted on the anode with yellow lines. Dimensions: LWH 0.2 × 28 × 18 cm.

© 2023 The Author(s). Published by the Royal Society of Chemistry

Open Access Article. Published on 06 marzu 2023. Downloaded on 17/10/2025 12:44:53.
This article is licensed under a Creative Commons Attribution 3.0 Unported Licence.

Table 1 Selected data for electro-corrosion reactions of iron. Standard Gibbs free energy (ΔG^{θ}) and entropic (ΔS^{θ}) values are from Bard *et al.*[31] n.r. is not reported

1	$Fe^{0}_{(s)} + H_2O \rightarrow Fe^{2+}O + H_{2(g)}$	$\Delta G^{\theta} = -14.3$ kJ mol^{-1}	$\Delta S^{\theta} = +94.2$ J K^{-1} mol^{-1}
2	$Fe^{0}_{(s)} + 2H_2O \rightarrow Fe^{2+}(OH)_2 + H_{2(g)}$	$\Delta G^{\theta} = -15.7$ kJ mol^{-1}	$\Delta S^{\theta} = +51.4$ J K^{-1} mol^{-1}
3	$Fe^{0}_{(s)} + 3H_2O \rightarrow Fe^{3+}(OH)_3 + 1.5H_{2(g)}$	$\Delta G^{\theta} = +6.4$ kJ mol^{-1}	$\Delta S^{\theta} = +63.5$ J K^{-1} mol^{-1}
4	$2Fe^{0}_{(s)} + 3H_2O \rightarrow Fe^{3+}{}_2O_3 + 3H_{2(g)}$	$\Delta G^{\theta} = -30.8$ kJ mol^{-1}	$\Delta S^{\theta} = +215.0$ J K^{-1} mol^{-1}
5	$3Fe^{2+}(OH)_{2(s)} \rightarrow (Fe^{3+}{}_2, Fe^{2+})O_4 + 2H_2O + H_{2(g)}$ Schikorr reaction	$\Delta G^{\theta} = -19.7$ kJ mol^{-1}	$\Delta S^{\theta} = +152.2$ J K^{-1} mol^{-1}
6	$2Fe^{3+}(OH)_{3(s)} \rightarrow Fe^{3+}{}_2O_3 + 3H_2O$	$\Delta G^{\theta} = -43.6$ kJ mol^{-1}	$\Delta S^{\theta} = +88.1$ J K^{-1} mol^{-1}
7	$4Fe^{2+}{}_{(aq)} + O_{2(aq)} + 4H^{+} \rightarrow 4Fe^{3+} + 2H_2O$	$\Delta G^{\theta} = -177.4$ kJ mol^{-1}	n.r.

$Fe_{(s)}$ from the electrodes and subsequent oxidation and selected thermodynamic data are given in Table 1.[30]

The electrode potentials for both oxidation processes are $Fe^{0}_{(s)} \rightarrow Fe^{2+}$, $E^{\circ} = +0.447$ V *vs.* SHE, and $Fe^{2+} \rightarrow Fe^{3+}$, $E^{\circ} = -0.771$ V *vs.* SHE.[32] Once leached ferrous (Reaction 1, Table 1) and ferric (Reaction 2, Table 1) iron is electromigrated towards the cathode, along the pH gradient, it eventually precipitates as, for example, magnetite (Fe_3O_4) through anaerobic corrosion in the Schikorr reaction (Reaction 5, Table 1). Electrochemically deposited magnetite at the surfaces of steel anodes may form in this way.[33–35] Given the historical and industrially sensitive nature of this work (performed under license in 2006) we do not have access to X-ray analysis on the resulting solids. In our view, however, the chemistry and therefore the likely phase mineralogy is not dissimilar from previous work by Cundy,[6] and Faulkner,[9] where X-ray diffraction showed that goethite, magnetite (and/or maghemite), lepidocrocite and other, amorphous iron (oxy)hydroxides were present, at modal abundances of up to 20%. In the bench-scale experiments, magnetite, haematite and maghemite were detected in the precipitated barrier material, although presence (or otherwise) of other Fe-rich phases could not be conclusively determined (based on authors' unpublished X-ray diffraction data).

The bench-scale and large-scale experiments show similar trends in current measurement over time (Fig. 7), whereby increases in current following addition of electrolyte are superimposed on a general decline in current over time, observed in both experimental systems.

This general decline in current over time is consistent with iron barrier formation, as growth of the (impermeable) deposits retards hydraulic (and ion) flow in the cells. This is in line with previous observations on a drop of initial current from 0.74 A to 0.14 A by Faulkner *et al.* in a 40 × 20 × 5 cm cell containing siliciclastic sand on application of a 3 V electric field over 19 days.[9] Notably, in this earlier paper, deliberate rupturing of the iron barrier led to an increase in current and subsequent regrowth/resealing of the barrier, indicating that the precipitated barrier can "self-heal" due to the re-established flow path between opposite polarity electrodes created by the rupture.

3.2 Effect of electrolyte on iron barrier growth, and barrier growth rate

Bench experiments undertaken with different electrolytes (but with constant voltage) show a clear dependence of barrier formation time on electrolyte strength. Fig. 8 shows the time taken to first observe the iron barrier, as well as the time taken to reach a 10 mm barrier thickness, which we consider sufficient thickness to reduce ground permeability and thus inhibit water flow at scale. The figure shows the temperature-adjusted electrical conductivity values for the 20, 100 and 500 ppm solutions, and tap water. No barrier formation was observed in the control experiments.

Higher electrolyte ionic strength leads to faster iron barrier growth due to enhanced corrosion and more rapid electrolysis. This is not surprising, as electrolytes of higher ionic strength are well-known to increase the soil current of an EKR deployment (*e.g.*, Li *et al.* and refs. therein).[36] Zakowski *et al.* have previously reported (2014) that higher salinities lead to enhanced corrosion rates of steel electrodes,[37] and the effect of higher salinities on increased corrosion rates of mild and other steels has been reported.[38,39] Here, for both the first appearance of the iron barrier and the time taken to grow to 10 mm, this effect is replicated, with the 500 ppm KCl electrolyte causing

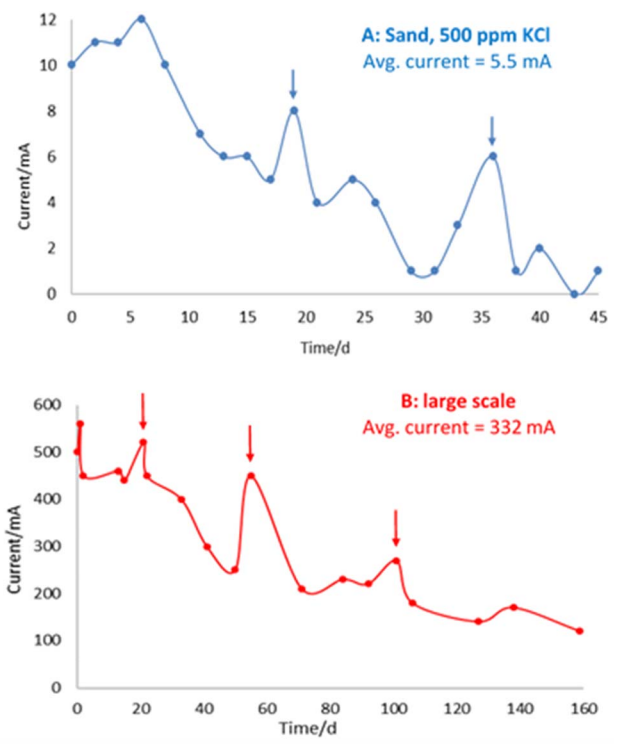

Fig. 7 A (top) and B (bottom) – Amperometry for cell with 500 ppm KCl in sand (top, "A") and large-scale experiment (bottom, "B"). Vertical arrows indicate addition of electrolyte and corresponding current increase. Avg. is average.

Open Access Article. Published on 06 marzu 2023. Downloaded on 17/10/2025 12:44:53.
This article is licensed under a Creative Commons Attribution 3.0 Unported Licence.

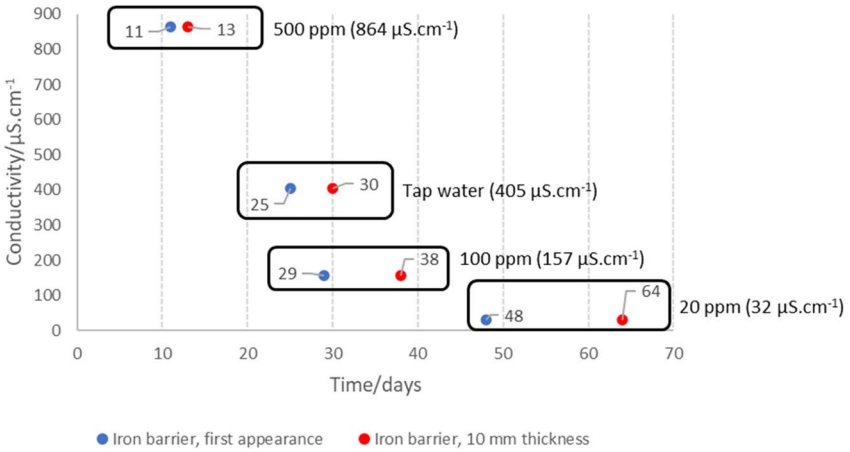

Fig. 8 Electrolyte electrical conductivity and time taken to first observe (in blue) the iron barrier material, and time taken to reach 10 mm thickness (red). The number of days is represented next to each data point, with common data points for each solution and the corresponding conductivity also highlighted. With 100 ppm KCl electrolyte, an average current of 1 mA was recorded, increasing to 2 mA for the tap water and 4 mA for the 500 ppm KCl electrolyte. No current (*e.g.* 0 mA) was recorded for the 20 ppm KCl electrolyte or controls (deionized water, tap water, 500 ppm KCl; no voltage), presumed to be below the detection threshold of our amperometer (1 mA resolution and detection threshold). For ease of visualisation, conductivity (the known variable) is plotted here on the *y*-axis, and time, the unknown variable, on the *x*-axis.

appearance of an iron barrier after 11 days, *vs.* 48 days for the 20 ppm KCl electrolyte (Fig. 8). Electrolyte strength also shifts the distance from the anode at which the iron barrier is precipitated; Fig. 9 shows the distance from the anode at which iron barriers form with each electrolyte used.

To investigate the iron barrier growth rate further, we examined barrier growth over time in the cell containing 500 ppm KCl electrolyte, Fig. 10. This was the cell with the highest average current and so most convenient to study over realistic experimental timescales.

For the cell with 500 ppm KCl electrolyte the final thickness of the iron barrier after 45 days was 55 mm at the thinnest point, extending 85 mm from the anode (*cf.* half of the 17 cm inter-electrode gap). Further, a thickness (21 mm) of iron barrier precipitated after only 24 days with this low voltage. As shown in Fig. 10, in our test system an iron barrier grows at a little over 1 mm per day (1.12 mm day^{-1} with R^2 correlation of 0.98). This is the first detailed examination of the growth rate of electrokinetically-grown iron barriers that we are aware of, and work is underway in our laboratories to expand both the scope and scale of these tests.

3.3 Power requirements and cost for scalable *in situ* barriers

The power, electricity and cost required to grow an iron barrier in each cell are given below in Table 2. This includes all small- and larger-scale experiments performed (Sections 2.2–2.3).

Based on these experiments and calculations EKR and *in situ* barrier formation could easily be scaled accordingly to much larger cells or systems. With inexpensive electrode materials

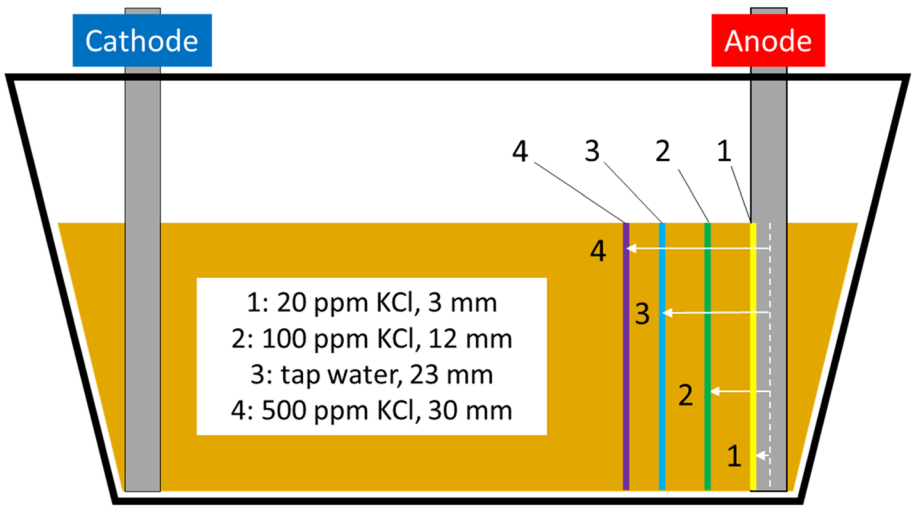

Fig. 9 Scaled schematic of the EKR test cells with lines showing distance from anode at which iron barrier material was first observed; 1 = 20 ppm KCl electrolyte, 2 = 100 ppm KCl electrolyte, 3 = tap water electrolyte, 4 = 500 ppm KCl electrolyte.

© 2023 The Author(s). Published by the Royal Society of Chemistry

Open Access Article. Published on 06 marzu 2023. Downloaded on 17/10/2025 12:44:53.
This article is licensed under a Creative Commons Attribution 3.0 Unported Licence.

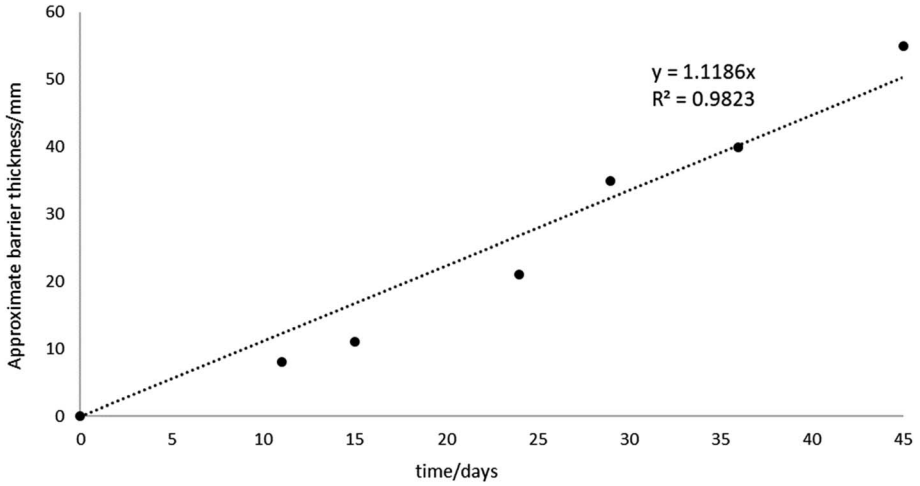

Fig. 10 Barrier growth over time, showing a strong correlation ($R^2 = 0.98$) between barrier thickness and time over which voltage is applied to the system (1.25 kg sand, LWH = 19 × 13 × 9 cm cells, 500 ppm KCl electrolyte at 10 V, or 0.53 V cm^{-1}).

Table 2 Calculated power requirements for EKR to generate the first appearance of an iron barrier, and a 10 mm thickness iron barrier, in different cells. No iron barrier was observed for control experiments

			Barrier appearance/days		Electricity consumed/kW h	
Electrolyte/experiment	Current[a]/A	Power/W	First	To 10 mm	First appearance	To 10 mm
Controls	No corrosion observed					
20 ppm KCl[c]	—[b]	—[b]	48	64	—[b]	—[b]
100 ppm KCl[c]	0.001	0.01	29	38	0.007	0.009
Tap water[c]	0.002	0.02	25	30	0.012	0.014
500 ppm KCl[c]	0.004	0.04	11	13	0.011	0.013
Large scale[d]	0.332	16.6	42	—[e]	16.733	—[e]

[a] Notes: average current measured across duration of experiments, to nearest mA. [b] Current for 20 ppm KCl electrolyte cell was consistently displayed as "0.000 A", presumed below the detection limit of our amperemeter. [c] 10 V over time in 19 cm long cell, variable electrolyte. [d] 50 V, 200 cm long cell, 1 mM $NaNO_3$ electrolyte. [e] Not reported or no data available. Power consumption was estimated from the voltage (given above), multiplied by the average current for each experiment (*e.g.*, $P = VI$; P is power, V is voltage and I is current).

and low power consumption, the setup and running costs of EKR are low, as demonstrated by Agnew *et al.* using 2011 figures where the treatment cost of Pu-contaminated soil was £1700 m^{-3} using EKR. This was in comparison to a cost of *ca.* £5000 m^{-3} for direct removal (excavation and disposal).[40]

Here, for the largest scale experiment (50 V, 200 cm length, 0.25 V cm^{-1}, Section 2.3) the total power consumed to first observe the iron barrier material is 16.6 W (from 0.332 A average current multiplied by 50 V) multiplied by 1008 hours (42 days). This gives a total electricity consumption of 16.7 kW h. Taking an average industrial electricity price in the UK of £0.11 per kW h for 2019,[41] this equates to just £1.84 (increasing to £4.17 if rates consistent with the 2021–2022 energy crisis are used); for the USA at average 2020 industrial prices of $0.07 per kWh, this is $1.17.[42] Even extending this out over the full duration of 160 days (3840 hours; 63.74 kW h), this still only equates to £7.01 or $4.46. By our estimation, therefore, the cost of electricity to successfully operate metre-plus scale cells for months is small, not more than single-digit or perhaps tens of GBP (£) or USD ($). The chief cost in our view is labor, and compared to conventional techniques such as excavation, much less labor is required to install and maintain EKR treatment cells. Consequently, we believe EKR combined with *in situ* barrier precipitation to be comparatively cost-competitive to existing techniques, although further work is needed on power consumption in scaled, *in situ*, systems.

4. Concluding remarks, further research requirements, and wider application

The data presented here clearly demonstrate that the deliberate generation of iron-rich barriers, grown from anode dissolution in real and simulated nuclear site materials, is feasible at up to and including the metre scale. We have demonstrated that barrier growth occurs over realistic timescales (days to months) at low voltages (typically <1 V cm^{-1}) and electrolyte strengths, in realistic nuclear site media (simulated and real Sellafield site sands), through the deposition of environmentally ubiquitous

Open Access Article. Published on 06 marzu 2023. Downloaded on 17/10/2025 12:44:53.
This article is licensed under a Creative Commons Attribution 3.0 Unported Licence.

non-hazardous ions (iron). Operating costs are inexpensive (*e.g.* tens of GBP/USD), and the system uses low-cost materials (mild steel). The system effectively mimics natural iron mineralization processes, where internal electric fields present in rock and soil bodies can generate multiple bands of ironstone *via* precipitation of Fe oxides and hydroxides.[43] Further investigations on solutions containing environmentally-relevant concentrations of dissolved solids (32 – 864 μS cm^{-1}) confirm that higher ionic strength electrolytes cause faster precipitation of iron-rich barriers, as expected from previous literature. These iron-rich materials and barriers are known to be sorptive, impermeable and useful in stabilizing soil.[6] We have demonstrated that the use of high-energy systems is unnecessary for the growth of iron-rich barriers in soil subsurfaces and that, in fact, low energy systems are feasible. This is a key result, as 'low intensity' (<1 mA cm^{-2}) cells are at worst environmentally benign (Gill *et al.* have previously assessed systems of this strength as having "no overall effect [on the microbial community]…")[44] and at best may actually facilitate enhanced land treatment (*e.g.* by increasing cellular metabolic rates).[45] Although high-energy electrokinetic systems may increase growth rate of iron-rich barriers they consume considerable energy, and often damage soil quality (for example, through extreme pH gradients, unwanted electrolysis of water, soil heating, microbial cellular deformation, or increased contaminant cytotoxicity).[46–48] The pH gradients generated in our test cells may inhibit soil bacterial activity close to the electrodes, but will dissipate following cessation of applied current, and where needed can be neutralized by polarity-switching at the electrodes at treatment termination, simulating methods used for pH regulation in existing electro-bioremediation approaches.[49]

With this in mind we believe the work described (and previously published data) highlights the potential for the practical application of this technology for subsurface contaminant management or stabilisation at nuclear and other sites, *via* physical trapping, *i.e.* hydraulic containment *via* groundwater flow manipulation at scale, or contaminant adsorption on the *in situ* iron phases. For the former, *in situ* trials under realistic vadose zone and groundwater flow conditions are required to show full proof of concept, and for the latter, while Fe-rich phases are known to be effective sorbents for a range of common nuclear site contaminants (*e.g.* Tc, Pu, and others[6]), further work is needed on the mineralogy of the precipitated barrier, and mechanisms of sorption or incorporation of different radionuclides (and the reversibility of this), under realistic site and groundwater conditions. A further issue requiring attention is the management of pore water, and flow, which may be required to prevent back flow of contaminated fluids. Similarly, the *in situ* stability and longevity of the iron precipitates forming the barriers needs site-specific evaluation to inform local Safety Cases, particularly where varying soil pH and fluid flow conditions are expected (*i.e.* where reducing or acid flows may impact the barrier following its precipitation). The two experimental studies described here, however, clearly demonstrate that barrier generation is possible in realistic subsurface materials at existing sites, including the shallow sub-surface on the UK's Sellafield site. We have previously assessed the Technology Readiness Level (TRL) of EKR with *in situ* mineral precipitation at TRL 4–7,[4] and the work described here reinforces this towards the higher end of this estimate; *e.g.*, towards an operational prototype in real systems. Feasibility of extending the process to lower permeability clayey soils (for example, contaminated forest soils in the Fukushima exclusion zone) has also been shown.[50]

We also note recent advances in the use of sacrificial anodes for soil, groundwater and wastewater treatment,[51] including iron[12,52–54] magnesium,[55] and aluminium.[56,57] A range of problematic contaminants are known to reductively precipitate in the presence of reduced iron minerals and phases, or sorb to iron-rich phases (and other metal oxides and oxyhydroxides, including those of Al).[54,58] This suggests further work on the chemistry and sorptive characteristics of electrokinetic barriers grown in authentic material should be a priority for further study, not only for iron, but also other commonly-occurring metals.

Author contribution

Jamie M. Purkis: conceptualization, methodology, validation, formal analysis, investigation, resources, data curation, writing – original draft, writing – review & editing, visualization, project administration. Frances Burrell: writing – review & editing, project administration. James R. Brydie: conceptualization, methodology, validation, formal analysis, investigation, resources, design, writing – review & editing, project administration. James Graham: writing – review & editing, project administration. Laurence Hopkinson: conceptualization, writing – review and editing. Andrew B. Cundy: conceptualization, methodology, resources, writing – review & editing, supervision, project administration, funding acquisition.

Conflicts of interest

The authors declare no competing financial or personal interests that influence this work.

Acknowledgements

The authors thank the NDA, NNL and predecessors as well as authors for kindly providing access to many reports described here. The authors also thank GAU-Radioanalytical at the University of Southampton for experimental support. Part of this work has been funded through the TRANSCEND (TRANsformative SCience and Engineering for Nuclear Decommissioning) consortium from the UK's Engineering and Physical Sciences Research Council, EPSRC (reference EP/S01019X/1). We also acknowledge support from the National Nuclear User Facility EXACT (Next Generation Accelerated Characterisation Technologies), *via* EPSRC grant EP/T011548/1. We thank two anonymous reviewers for comments that improved the overall discussion of the data presented and its wider implications.

© 2023 The Author(s). Published by the Royal Society of Chemistry

Open Access Article. Published on 06 marzu 2023. Downloaded on 17/10/2025 12:44:53.
This article is licensed under a Creative Commons Attribution 3.0 Unported Licence.

References

1 Y. B. Acar, R. J. Gale, A. N. Alshawabkeh, R. E. Marks, S. Puppala, M. Bricka and R. Parker, Electrokinetic remediation: Basics and technology status, *J. Hazard. Mater.*, 1995, **40**, 117–137.
2 K. R. Reddy and S. Chinthamreddy, Electrokinetic remediation of heavy metal-contaminated soils under reducing environments, *Waste Manag.*, 1999, **19**, 269–282.
3 C. Cameselle and S. Gouveia, Electrokinetic remediation for the removal of organic contaminants in soils, *Curr. Opin. Electrochem.*, 2018, **11**, 41–47.
4 J. M. Purkis, P. E. Warwick, J. Graham, S. D. Hemming and A. B. Cundy, Towards the application of electrokinetic remediation for nuclear site decommissioning, *J. Hazard. Mater.*, 2021, **413**, 125274.
5 A. B. Cundy and L. Hopkinson, Method for Soil Remediation and Engineering, *GB Patent*, GB0222393D0, 2002.
6 A. B. Cundy and L. Hopkinson, Electrokinetic iron pan generation in unconsolidated sediments: implications for contaminated land remediation and soil engineering, *Appl. Geochem.*, 2005, **20**, 841–848.
7 C. H. Lai, S. L. Lo and C. F. Lin, Mechanisms of iron oxide coating onto sand surface and its adsorption behaviors for copper, *Toxicol. Environ. Chem.*, 1994, **46**, 107–118.
8 B. Rusch, K. Hanna and B. Humbert, Coating of quartz silica with iron oxides: Characterization and surface reactivity of iron coating phases, *Colloids Surf., A*, 2010, **353**, 172–180.
9 D. W. S. Faulkner, L. Hopkinson and A. B. Cundy, Electrokinetic generation of reactive iron-rich barriers in wet sediments: implications for contaminated land management, *Mineral. Mag.*, 2005, **69**, 749–757.
10 J. Shahabpour, Liesegang blocks from sandstone beds of the Hojedk Formation, *Geomorphology*, 1998, **22**, 93–106.
11 H. C. B. Hansen, Composition, stabilization, and light absorption of Fe(II)Fe(III) hydroxy-carbonate ('green rust'), *Clay Miner.*, 1989, **24**, 663–669.
12 L. Hopkinson, A. B. Cundy, D. W. S. Faulkner, A. Hansen and R. Pollock, Electrokinetic stabilization of Cr(VI)-contaminated soils, in *Electrochemical Remediation Technologies for Polluted Soils, Sediments and Groundwater*, ed. K. Reddy and C. Cameselle, John Wiley and Sons, Inc., New York, 2009, ch. 8, pp. 179–193.
13 X. Li, L. Liu, Y. Wu and T. Liu, Determination of the Redox Potentials of Solution and Solid Surface of Fe(II) Associated with Iron Oxyhydroxides, *ACS Earth Space Chem.*, 2019, **3**, 711–717.
14 Y. Gossuin, J.-M. Colet, A. Roch, R. N. Muller and P. Gillis, Cesium Adsorption in Hydrated Iron Oxide Particles Suspensions: An NMR Study, *J. Magn. Reson.*, 2002, **157**, 132–136.
15 P. Trivedi and L. Axe, A Comparison of Strontium Sorption to Hydrous Aluminum, Iron, and Manganese Oxides, *J. Colloid Interface Sci.*, 1999, **218**, 554–563.
16 A. D. Ebner, J. A. Ritter and J. D. Navratil, Adsorption of Cesium, Strontium, and Cobalt Ions on Magnetite and a Magnetite–Silica Composite, *Ind. Eng. Chem. Res.*, 2001, **40**, 1615–1623.
17 C. I. Pearce, R. C. Moore, J. W. Morad, R. M. Asmussen, S. Chatterjee, A. R. Lawter, T. G. Levitskaia, J. J. Neeway, N. P. Qafoku, M. J. Rigali, S. A. Saslow, J. E. Szecsody, P. K. Thallapally, G. Wang and V. L. Freedman, Technetium immobilization by materials through sorption and redox-driven processes: A literature review, *Sci. Total Environ.*, 2020, **716**, 132849.
18 D. Li and D. I. Kaplan, Sorption coefficients and molecular mechanisms of Pu, U, Np, Am and Tc to Fe (hydr)oxides: A review, *J. Hazard. Mater.*, 2012, **243**, 1–18.
19 E. J. O'Loughlin, S. D. Kelly, R. E. Cook, R. Csencsits and K. M. Kemner, Reduction of Uranium(VI) by Mixed Iron(II)/Iron(III) Hydroxide (Green Rust): Formation of UO2 Nanoparticles, *Environ. Sci. Technol.*, 2003, **37**, 721–727.
20 D. C. Girvin, L. L. Ames, A. P. Schwab and J. E. McGarrah, Neptunium adsorption on synthetic amorphous iron oxyhydroxide, *J. Colloid Interface Sci.*, 1991, **141**, 67–78.
21 K. Nakata, S. Nagasaki, S. Tanaka, Y. Sakamoto, T. Tanaka and H. Ogawa, Sorption and reduction of neptunium(V) on the surface of iron oxides, *Radiochim. Acta*, 2002, **90**, 665–669.
22 K. F. Smith, K. Morris, G. T. W. Law, E. H. Winstanley, F. R. Livens, J. S. Weatherill, L. G. Abrahamsen-Mills, N. D. Bryan, J. F. W. Mosselmans, G. Cibin, S. Parry, R. Blackham, K. A. Law and S. Shaw, Plutonium(IV) Sorption during Ferrihydrite Nanoparticle Formation, *ACS Earth Space Chem.*, 2019, **3**, 2437–2442.
23 B. E. Cowie, J. M. Purkis, J. Austin, J. B. Love and P. L. Arnold, Thermal and Photochemical Reduction and Functionalization Chemistry of the Uranyl Dication, $[UVIO_2]^{2+}$, *Chem. Rev.*, 2019, **119**, 10595–10637.
24 *CRC Handbook of Chemistry and Physics*, ed. W. M. Haynes, Taylor and Francis Group, Boca Raton, Florida, USA, 95th edn, 2015.
25 E. Lacasa, S. Cotillas, C. Saez, J. Lobato, P. Canizares and M. A. Rodrigo, Environmental applications of electrochemical technology. What is needed to enable full-scale applications?, *Curr. Opin. Electrochem.*, 2019, **16**, 149–156.
26 R. López-Vizcaíno, V. Navarro, M. J. Léon, C. Risco, M. A. Rodrigo, C. Sáez and P. Canizares, Scale-up on electrokinetic remediation: Engineering and technological parameters, *J. Hazard. Mater.*, 2016, **315**, 135–143.
27 U.S. Geological Survey, Specific conductance, chap. A6.3 (Section A, National Field Manual for the Collection of Water-Quality Data), in *U.S. Geological Survey Techniques and Methods*, 2019, DOI: **10.3133/tm9A6.3**.
28 J. Graham, MSSS GEMS Phase 2: Characterisation of Soils and Strontium Sorption Batch Testing, *Report NNL 13224*, National Nuclear Laboratory, NNL, 2015.
29 N. Takeno, Atlas of Eh-pH diagrams, *Geological Survey of Japan Open File Report No.419*, 2005.
30 A. Groysman, *Corrosion for Everybody*, Springer, Dordrecht, The Netherlands, 2010.

Open Access Article. Published on 06 marzu 2023. Downloaded on 17/10/2025 12:44:53.
This article is licensed under a Creative Commons Attribution 3.0 Unported Licence.

31 *Standard Potentials in Aqueous Solutions*, ed. A. J. Bard, R. Parsons and J. Jordan, International Union of Pure and Applied Chemistry, IUPAC, and Marcel Dekker, Inc., New York, USA/Basel, Switzerland, 1985.
32 D. A. Jones, *Principles and Prevention of Corrosion*, Pearson Eductation, 2nd edn, 2001.
33 L. Cabrera, S. Gutierrez, N. Menendez, M. P. Morales and P. Herrasti, Magnetite nanoparticles: Electrochemical synthesis and characterization, *Electrochim. Acta*, 2008, **53**, 3436–3441.
34 A. Rodríguez-López, A. Paredes-Arroyo, J. Mojica-Gomez, C. Estrada-Arteaga, J. J. Cruz-Rivera, C. G. Elías Alfaro and R. Antaño-López, Electrochemical synthesis of magnetite and maghemite nanoparticles using dissymmetric potential pulses, *J. Nanopart. Res.*, 2012, **14**, 993.
35 M. Starowicz, P. Starowicz, J. Żukrowski, J. Przewoźnik, A. Lemański, C. Kapusta and J. Banaś, Electrochemical synthesis of magnetic iron oxide nanoparticles with controlled size, *J. Nanopart. Res.*, 2011, **13**, 7167–7176.
36 D. Li, X.-Y. Tan, X.-D. Wu, C. Pan and P. Xu, Effects of electrolyte characteristics on soil conductivity and current in electrokinetic remediation of lead-contaminated soil, *Sep. Purif. Technol.*, 2014, **135**, 14–21.
37 K. Zakowski, M. Narozny, M. Szocinski and K. Darowicki, Influence of water salinity on corrosion risk—the case of the southern Baltic Sea coast, *Environ. Monit. Assess.*, 2014, **186**, 4871–4879.
38 R. E. Melchers, Predicting long-term corrosion of metal alloys in physical infrastructure, *npj Mater. Degrad.*, 2019, **3**, 4.
39 Z. Zeng, R. S. Lillard and H. Cong, Effect of Salt Concentration on the Corrosion Behavior of Carbon Steel in CO_2 Environment, *Corrosion*, 2016, **72**, 805–823.
40 K. Agnew, A. B. Cundy, L. Hopkinson, I. W. Croudace, P. E. Warwick and P. Purdie, Electrokinetic remediation of plutonium-contaminated nuclear site wastes: Results from a pilot-scale on-site trial, *J. Hazard. Mater.*, 2011, **186**, 1405–1414.
41 **https://www.gov.uk/government/statistical-data-sets/international-industrial-energy-prices**, (accessed 23rd November 2020).
42 U. S. E. I. Administration, *Monthly Electric Power Industry Report, Report Form EIA-861M*, 2020.
43 K.-H. Jacob, S. Dietrich, H.-J. Krug, Self organised mineral fabrics. in *Fractals and Dynamic Systems in Geoscience*, ed. J. H. Kruhl, Springer-Verlag, Berlin, 1996, pp. 259–268.
44 R. T. Gill, M. J. Harbottle, J. W. N. Smith and S. F. Thornton, Electrokinetic-enhanced bioremediation of organic contaminants: A review of processes and environmental applications, *Chemosphere*, 2014, **107**, 31–42.
45 N. Velasco-Alvarez, I. Gonzalez, P. Damian-Matsumura and M. Gutierrez-Rojas, Enhanced hexadecane degradation and low biomass production by Aspergillus niger exposed to an electric current in a model system, *Bioresour. Technol.*, 2011, **102**, 1509–1515.
46 J. C. Thrash and J. D. Coates, Review: Direct and Indirect Electrical Stimulation of Microbial Metabolism, *Environ. Sci. Technol.*, 2008, **42**(11), 3921–3931.
47 Q. Luo, X. Zhang, H. Wang and Y. Qian, Mobilization of phenol and dichlorophenol in unsaturated soils by non-uniform electrokinetics, *Chemosphere*, 2005, **59**(9), 1289–1298.
48 G. Lear, M. J. Harbottle, G. Sills, C. J. Knowles, K. T. Semple and I. P. Thompson, Impact of electrokinetic remediation on microbial communities within PCP contaminated soil, *Environ. Pollut.*, 2007, **146**, 139–146.
49 Q. Luo, X. Zhang, H. Wang and Y. Qian, The use of non-uniform electrokinetics to enhance in situ bioremediation of phenol-contaminated soil, *J. Hazard. Mater.*, 2005, **121**, 187–194.
50 J. M. Purkis, A. Tucknott, I. W. Croudace, P. E. Warwick and A. B. Cundy, Enhanced electrokinetic remediation of nuclear fission products in organic-rich soils, *Appl. Geochem.*, 2021, **125**, 104826.
51 J. Deborde, P. Refait, P. Bustamante, C. Caplat, O. Basuyaux, A.-M. Grolleau, M.-L. Mahaut, C. Brach-Papa, J.-L. Gonzalez and S. Pineau, Impact of Galvanic Anode Dissolution on Metal Trace Element Concentrations in Marine Waters, *Water, Air, Soil Pollut.*, 2015, **226**, 423.
52 A. A. G. D. Amarasooriya and T. Kawakami, Electrolysis removal of fluoride by magnesium ion-assisted sacrificial iron electrode and the effect of coexisting ions, *J. Environ. Chem. Eng.*, 2019, **7**, 103084.
53 M. Kobya, E. Demirbas and A. Akyol, Electrochemical treatment and operating cost analysis of textile wastewater using sacrificial iron electrodes, *Water Sci. Technol.*, 2009, **60**, 2261–2270.
54 J. Kumpiene, K. Engstrom, A. Pinedo Taquia, I. Carabante and J. Bjuhr, Arsenic immobilisation in soil using electricity-induced spreading of iron in situ, *J. Environ. Manage.*, 2023, **325**, 116467.
55 D. J. Kruk, M. Elektorowicz and J. A. Oleszkiewicz, Struvite precipitation and phosphorus removal using magnesium sacrificial anode, *Chemosphere*, 2014, **101**, 28–33.
56 A. Loukanov, N. El Allaoui, A. Omor, F. Z. Elmadani, K. Bouayad and S. Nakabayashi, Large-scale removal of colloidal contaminants from artisanal wastewater by bipolar electrocoagulation with aluminum sacrificial electrodes, *Results Chem.*, 2020, **2**, 100038.
57 N. El Allaoui, A. Omor, F. Z. Elmadani, K. Bouayad, S. Nakabayashi and A. Loukanov, Semi-industrial remediation of effluents polluted by the artisanal activities through bipolar electrocoagulation with aluminum sacrificial electrodes, *Water Environ. J.*, 2020, **34**(S1), 831–840.
58 L. Onnby, C. Svensson, L. Mbundi, R. Busquets, A. B. Cundy and H. Kirsebom, g-Al2O3-based nanocomposite adsorbents for arsenic(V) removal: assessing performance, toxicity and particle leakage, *Sci. Total Environ.*, 2014, **473–474**, 207–214.

© 2023 The Author(s). Published by the Royal Society of Chemistry